Proton-exchange in a paramagnetic chemical exchange saturation transfer agent from experimental studies and ab initio metadynamics simulation

Rodolphe Pollet, Celia Bonnet, Pascal Retailleau, Philippe Durand, Éva Tóth

Proton-exchange in a paramagnetic chemical exchange saturation transfer agent from experimental studies and ab initio metadynamics simulation

Rodolphe Pollet,[*,†] Célia S. Bonnet,[‡] Pascal Retailleau,[¶] Philippe Durand,[¶] and Éva Tóth[‡]

†*NIMBE, CEA, CNRS, Université Paris-Saclay, CEA Saclay, 91191 Gif-sur-Yvette Cedex, France*

‡*Centre de Biophysique Moléculaire, CNRS UPR 4301, Université d'Orléans, rue Charles Sadron, 45071 Orléans 2, France*

¶*Institut de Chimie des Substances Naturelles, CNRS UPR 2301, Université Paris-Saclay, 1 av. de la Terrasse, 91198 Gif-sur-Yvette, France*

E-mail: rodolphe.pollet@cea.fr

Abstract

The proton exchange process between water and a carbamate has been studied experimentally and theoretically in a lanthanide-based paramagnetic chemical exchange saturation transfer agent endowed with potential multimodality detection capabilities (optical imaging, or T_1 MRI for the Gd(III) analogue). In addition to an in-depth structural analysis by a combined approach (using X-ray crystallography, NMR, and molecular dynamics), our *ab initio* simulation in aqueous solution sheds light on the reaction mechanism for this proton exchange which involves structural Grotthuss diffusion.

Introduction

During the 1980s, the first generation of MRI contrast agents emerged with the ability to accelerate the relaxation process of surrounding water protons. Still widely used in clinical applications, these are mainly gadolinium(III) chelates acting as T_1 Paramagnetic Relaxation Enhancement (PRE) contrast agents. A new class of MRI probes that could challenge this approach operates in a completely different way. In the chemical exchange saturation transfer (CEST) mechanism, the bulk magnetization of a given type of protons (A) becomes perturbed (i.e., reduced) because of the exchange with another type of protons (B) that have been presaturated.[1–5] When protons A are those of tissue water, the decrease of the signal intensity produces negative image contrast. In comparison with conventional T_1 PRE contrast agents, probes based on this CEST effect have the advantage to be switchable by the presaturation pulse. Another interesting feature of CEST imaging is that several CEST agents can be simultaneously visualized on the same image if their resonance frequency is different. Since the "slow-to-intermediate exchange" condition $\Delta\omega \geq k_{ex}$ (where $\Delta\omega$ is the frequency difference between A and B, and k_{ex} is the exchange constant) must be obeyed while the exchange must be as fast as possible (to accelerate saturation transfer and counter relaxation), paramagnetic complexes of lanthanide ions can be used to increase $\Delta\omega$ up to a few hundred ppm from the bulk water signal (through hyperfine shifts), resulting in so-called paraCEST agents. Furthermore, these probes can be made responsive to pH, temperature, enzyme activity, or biomarkers, hence becoming "smart" agents.[3–5]

Exchangeable protons of paraCEST agents do not necessarily belong to a bound water molecule. Instead, amide, amine and alcohol protons on the pendant arms of macrocyclic ligands can be sufficiently hyperfine shifted to be suitable for CEST imaging.[6] Recently, CEST effect was also reported for carbamate protons of a lanthanide based platform endowed with potential multimodality.[7] The present work will be mainly devoted to the molecular simulation of this platform, i.e., a DO3A derivative substituted by a (6-methylpyridin-2-yl)carbamate, coordinated to the europium(III) cation (see Figure 1). More specifically we will focus on the paraCEST properties of this complex (EuL) through investigation of the carbamate hydrogen exchange reaction with water hydrogens.

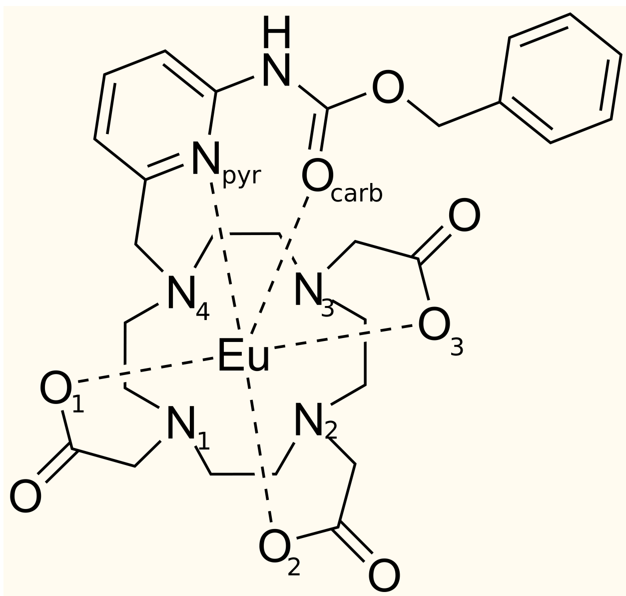

Figure 1: EuL, Europium(III) complex of a DO3A derivative substituted by a benzyl (6-methylpyridin-2-yl)carbamate.

Over the years, we have developed a strong expertise in the field of *ab initio* simulation of contrast agents based on lanthanide ions. Our first paper in the series was devoted to the structure and hydrogen-bonded network of [Gd(HPDO3A)(H_2O)] in aqueous solution, a paramagnetic gadolinium(III) complex used in clinical applications of MRI.[8] Then the water exchange reaction governing the contrast enhancement power of two of its isomers was studied, explaining the dissociative mechanism and estimating the corresponding reaction barriers.[9] More recently, its time-dependent magnetic properties, including hyperfine tensors[10] and zero-field-splitting,[11] were investigated. In the present work, we again rely on such first-principles approach, applying the same theoretical method that we used for the free-energy landscape of the water exchange reaction, namely, *ab initio* metadynamics. This sampling technique indeed allows the crossing of high free-energy barriers along the minimum free-energy path as well as the reconstruction of the free-energy hypersurface.[12,13] Here we emphasize that in contrast to our previous work, the proton-exchange reaction in the paraCEST agents involves the breaking of a covalent bond (the NH bond). Taking into account the electronic structure during the molecular dynamics simulation is therefore more crucial than ever.

This theoretical interest has been initially inspired by a detailed experimental work including the design, synthesis and physico-chemical characterization of the lanthanide complexes of this carbamate derivative ligand in the context of enzymatic detection by paraCEST agents.[7] To complete the theoretical approach, we have thus synthesized EuL, solved the X-ray structure, and recorded ^{1}H NMR and paraCEST spectra (see details in the following section and in the Supporting Information).

Experimental section

The europium complex, EuL, was synthesized from the free ligand and europium chloride as previously reported for the gadolinium analogue.[7] The compound was analyzed by LC-MS and NMR.

In order to determine the complex structure in solid state, a colourless crystalline stick of the complex EuL, obtained by vapour diffusion of acetone solvent into aqueous solution, was glued to a tip of glass pin then transferred to an Enraf-Nonius kappaCCD diffractometer, using graphite monochromated Mo-Kα($\lambda = 0.71073$ Å) radiation. A full hemisphere of data (ϕ-scan) completed by a couple of other ω-scans[14,15] were collected at room temperature, then integrated and corrected for Lorentz, polarization, and absorption effects using SCALEPACK.[14] The space group was univocally assigned to be P2_1 (nr 4). The structure was solved by direct methods (SHELXS-97)[16] and expanded through successive difference

Fourier maps. It was refined against all data except three low-resolution reflexions shaded by the beamstop, using SHELXL-2014/7.[17] Thermal parameters for all non-hydrogen atoms were refined anisotropically. Hydrogen atoms were mainly located in the difference Fourier maps but those attached to carbon atoms were refined using a riding model whereas the N-H distance was refined with restraint of 0.87 (2) Å. The water hydrogen atoms were also spotted in Fourier residuals and their geometric parameters were restrained (DFIX 0.83 (2) and DANG 1.33 (4) Å instructions) in order to form an optimal H-bond network. The hydrogen isotropic thermal parameters were defined as 1.2 times that of the carrier atom (1.5 for water oxygen). Absolute structure was assessed by the Flack parameter $x = -0.036(8)$ determined using 3712 quotients by the Parsons method.[18]

^{1}H NMR data reveal the presence of two stereoisomers in solution which are present in comparable ratio (see Supporting Information). Since the *ab initio* metadynamics simulation is highly demanding, the present work focuses only on the twisted capped square antiprismatic (TSAP) isomer, which is the isomer found in the solid state (see below). The paraCEST spectra of the complex EuL (19.9 mM; pH 7.4 or 6.4, 310 K) were recorded in H_2O/D_2O (95/5 (v/v)) at 400 MHz on a Bruker Advance Spectrometer using a 5 mm BBFO probe using a pre-saturation pulse of 3 s at a saturation power of $B = 1030$ Hz. They were obtained by plotting the bulk water signal intensity as a function of the saturation frequency in a window scale of 100 ppm saturating at each 0.5 ppm. The spectrum recorded at pH 7.4 exhibits a CEST peak at 11 ppm, which is relatively large and very likely is hiding two CEST effects related to the two isomers in solution (see Figure 2). When reducing the temperature or the saturation power, the presence of two CEST effects becomes more evident. However, even at 298 K and $B = 515$ Hz, they cannot be separated (see Figure S6). The two carbamate protons resulting in the CEST effect could be indeed identified in the ^{1}H NMR spectrum recorded in H_2O/D_2O (80/20 (v/v), pH 4.6) at the corresponding frequencies (see Figures S3-4). We note that in CEST spectra, the water peak is conventionally set to 0 ppm, whereas in the NMR spectra it is at 4.7 ppm which explains the difference in the resonance frequencies

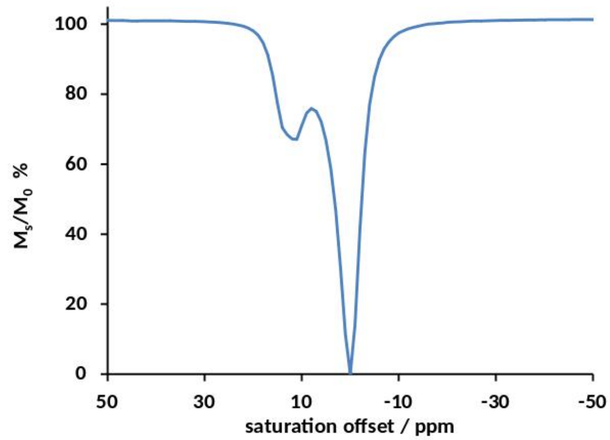

Figure 2: CEST spectrum of the europium complex EuL (19.9 mM; pH 7.4), recorded in H_2O/D_2O (95/5 (v/v)) at 400 MHz. The saturation time was 3 s and the saturation power was $B = 1030$ Hz.

between the CEST and the ^{1}H NMR spectrum. To determine the proton exchange constant, QUESP (QUantification of the Exchange rate by modulating the Saturation Power) experiments were performed by varying the saturation power between 0.18 and 76 μT (0.07 and 20 mW) and keeping a constant saturation time of 3 s. Measurements were done at pH 7.4 and 6.4. The QUESP data have been analyzed by the concentration-independent "omega-plot" method reported by Dixon et al.[19] and by the Hannes-Woolf HW-QUESP method.[20] In the "omega-plot" method, a plot of $M_S/(M_0 - M_S)$ versus $1/\omega_1^2$ (referred to as omega plot) should be linear, with an X-axis intercept ($M_S/(M_0 - M_S) = 0$) providing a direct readout of the exchange rate constant, $-1/k_{ex}^2 = 1/\omega_1^2$:

$$\frac{M_S}{M_0 - M_S} = \frac{55.5}{c} k_{ex} R_{1w} \left(\frac{1}{k_{ex}^2} + \frac{1}{\omega_1^2} \right) \quad (1)$$

Here M_S is the signal intensity of the bulk water protons taken immediately after the pulse is applied to the exchangeable protons of the CEST agent, M_0 is the initial intensity of bulk water protons in the absence of saturation, k_{ex} is the proton exchange rate constant, c is the concentration of the CEST agent, R_{1w} is the longitudinal relaxation rate of the bulk water in the saturated state and ω_1 is the amplitude of the radiofrequency applied for the saturation pulse given in radians/second. The Hannes-Woolf QUESP method (HW-QUESP) is derived from the omega-plot method and is also independent of the concentration,

$$\frac{\omega_1^2 M_S}{M_0 - M_S} = \frac{\omega_1^2 R_1}{\chi_{CA} k_{ex}} + \frac{R_1 k_{ex}}{\chi_{CA}} \tag{2}$$

A plot of $\omega_1^2 M_S/(M_0 - M_S)$ as a function of ω_1^2 is a straight line, with an intercept of the X-axis that gives access to the square of the proton exchange rate constant, $-k_{ex}^2 = \omega_1^2$. The two methods gave identical values within statistical error (see Figure S9).

Computational details and preliminary calculations

All plane-waves DFT calculations have been based on the unrestricted Kohn-Sham scheme with PBE exchange-correlation approximation.[21] Large core ultrasoft pseudopotentials[22] including scalar relativistic effects have been specifically designed for europium in order to reduce the computational cost of the *ab initio* molecular dynamics simulation in aqueous solution. Geometry optimizations in gas phase have been first performed as preliminary tests, varying the cutoff energy and probing the influence of a D2 dispersion correction[23] (see Table 1). This has been followed by a Car-Parrinello (CP)[24,25] simulation in aqueous solution, with the Eu(III) complex in a 18 Å cubic box including 152 water molecules. Other parameters include a fictitious electron mass of 700 a.u., a time step of 6 a.u., and Nosé–Hoover chain thermostats (with a chain length of three) both for ions (with the target temperature set to 310 K) and electrons in order to prevent heat transfer between both subsystems. To this aim, hydrogen atoms have also been replaced by deuterium atoms. The averaged distances reported in Table 1 have been obtained by only keeping the last 30 ps of a 126 ps trajectory. Besides, a strong hydrogen bond has been formed between NH and a water molecule, with an average N–O distance of 2.92 Å. However no proton transfer has been observed at this stage.

At this point we can observe that the coordination cage closes and the capping carba-

Table 1: Distances (in Å) between Eu(III) and coordinated atoms from experiment (see Supporting Information for crystallographic details) and DFT calculations performed at 30 Ry with ultrasoft pseudopotentials: geometry optimizations (opt) in gas phase with or without D2 dispersion correction, Car-Parrinello (CP) and metadynamics (MTD) simulation at 310 K in aqueous solution. The numbering of the atoms refers to Figure 1.

	Eu-O_{carb}	Eu-N_{pyr}	Eu-O_1	Eu-O_2	Eu-O_3	Eu-N_1	Eu-N_2	Eu-N_3	Eu-N_4
exp (X-ray)	2.44	2.70	2.38	2.37	2.36	2.66	2.64	2.73	2.67
opt (PBE)	2.47	2.76	2.32	2.28	2.36	2.73	2.74	2.89	2.83
opt (PBE+D2)	2.47	2.77	2.32	2.27	2.36	2.74	2.74	2.91	2.83
CP (PBE+D2)	2.54	2.72	2.43	2.37	2.40	2.73	2.78	2.79	2.73
MTD (PBE+D2)	2.59	2.75	2.45	2.36	2.37	2.71	2.75	2.80	2.73

mate oxygen is farther from europium in aqueous solution than in gas phase. The N_{pyr}-Eu-O_2 and O_1-Eu-O_3 angles indeed decrease from 142 and 145 degrees in gas phase to 139 and 141 degrees in liquid water, respectively. Simultaneously the Eu-O_{carb} distance increases from 2.47 to 2.54 Å. This is consistent with the dissociative mechanism found for the [Gd(HPDO3A)(H_2O)] isomers where the closing of the coordination cage and the detachment of the inner-sphere water are interrelated.[9]

From this equilibrated CP trajectory, a metadynamics simulation has been conducted to efficiently explore the free-energy landscape of the proton-exchange reaction. To this aim, two collective variables (CVs) have been selected, namely, the coordination numbers (CNs) of N with respect to its initial proton (CV1) and to all water protons (CV2). In both cases, the following expression has been used:[26,27]

$$CN = \sum_i \frac{1-(d_i/d_0)^p}{1-(d_i/d_0)^{p+q}} \tag{3}$$

where d_i is the distance between N and the i^{th} hydrogen, $d_0 = 1.6$ Å, $p = 8$ and $q = 8$. In addition, an extended Lagrangian formalism has been used to slowly propagate auxiliary variables that drag these two CVs away thanks to a harmonic coupling[27,28] with coupling constants k set to 2.0 and fictitious masses to 50 a.u. The width and height of the Gaussians deposed on the free-energy surface were respectively set to 0.03 u.s and 0.001 a.u. (i.e., approximately 1 k_BT) up to the point where the NH bond breaking was about to occur (here after 202 Gaussians), where the hills height was changed to 1/4 k_BT. The metadynamics time step was actually not constant. Instead, it was determined on-the-fly to avoid "hill surfing".[29] Moreover the temperature of the auxiliary variables was bound to fluctuate in the 310 $\pm$ 200 K range thanks to a simple scaling of the velocities. Our simulation was stopped after more than 5000 Gaussians accumulated, when all the free-energy basins have been correctly sampled.

Results and discussions

Thermodynamic studies

The free-energy surface obtained from our *ab initio* metadynamics trajectory exhibits two main basins separated by a large intermediate region (see Figure 3). The pathway from one basin to the other is almost linear (i.e., the second CV is almost constant). The deepest basin actually contains two degenerate free-energy minima respectively located at coordinates (0.96,0.02) and (1.00,0.00). However it is not entirely clear whether this degeneracy corresponds to different orientations of the hydrogen-bonded water molecule or if this is an artifact due to the larger size of the hills at the beginning of the simulation. Escaping from this basin leads to a transition state 58 kJ/mol above these minima, at coordinates (0.72,0.02). The agreement with the experiment is good since a free-energy barrier of 54 kJ/mol can be deduced (using Eyring equation) from the experimentally determined proton-exchange rate constant (of 6100 ± 500 s^{-1} at pH 7.4 and 310 K). One should keep in mind, however, that the Eyring equation is an exponential function and a difference of 4 kJ/mol in the free energy translates to a six-fold variation in k_{ex}, which nevertheless remains in the same order of magnitude. We note that the good agreement between the calculated k_{ex} and the experimental proton exchange rate constant, which represents an average value for the two isomers, suggests that the proton exchange rates on the two isomers should be in the same order of magnitude. The observation of two CEST effects also corroborates the fact that the proton exchange cannot be very different for the two isomers (if k_{ex} was much higher or much lower on one of the isomers, only one CEST effect would be observable). This is confirmed by following the variation of peak width at half height in the ^{1}H NMR spectra as a function of temperature (see Figure S5). This study indicates that line-broadening of the exchangeable H (see Table S1 and Figure S5) is dominated by the exchange with water (the broadening due to the interconversion between SAP and TSAP isomers can be neglected in a first approximation). Upon heating, peak broadening for both exchangeable protons is in the same range, suggesting that the exchange rate is quite similar (at least it is in the same order of magnitude) for the two isomers. At pH 6.4, the exchange rate constant is 1900 ($\pm$500) s^{-1} (see Figure S10), about three times lower that at pH 7.4, implying a base-catalyzed proton exchange, as it can be expected for a carbamate proton, in analogy to amide protons.

The second free-energy basin is very broad along CV2 but precisely centered at $CV1 = 0$, which corresponds to a complete detachment of the inital NH proton. This broad distribution is due to the absence of a strong covalent bond between N and the other protons. In contrast, protons which are candidates to a coordination to N are alternatively shared, hydrogen-bonded, or too far from nitrogen, which results in a distance amplitude approximately 15 times larger with reference to the initial situation. An accurate localization of its free-energy minimum is therefore not possible. Escaping it requires a free-energy of approximately 47 kJ/mol, with a transition state located at coordinates (0.08,0.02).

Structural study

The solved X-ray structure of the complex EuL shows the presence of five water molecules in the near environment of the complex in the solid state but none in the inner sphere of the metal. L was found coordinate to the central ion in a nonadentate fashion, with the pyridine pendant arm forming a five-membered chelate ring and the carbamoyl pendant arm forming a six-membered chelate ring. The configurations of the pendant arms and of the macrocyclic

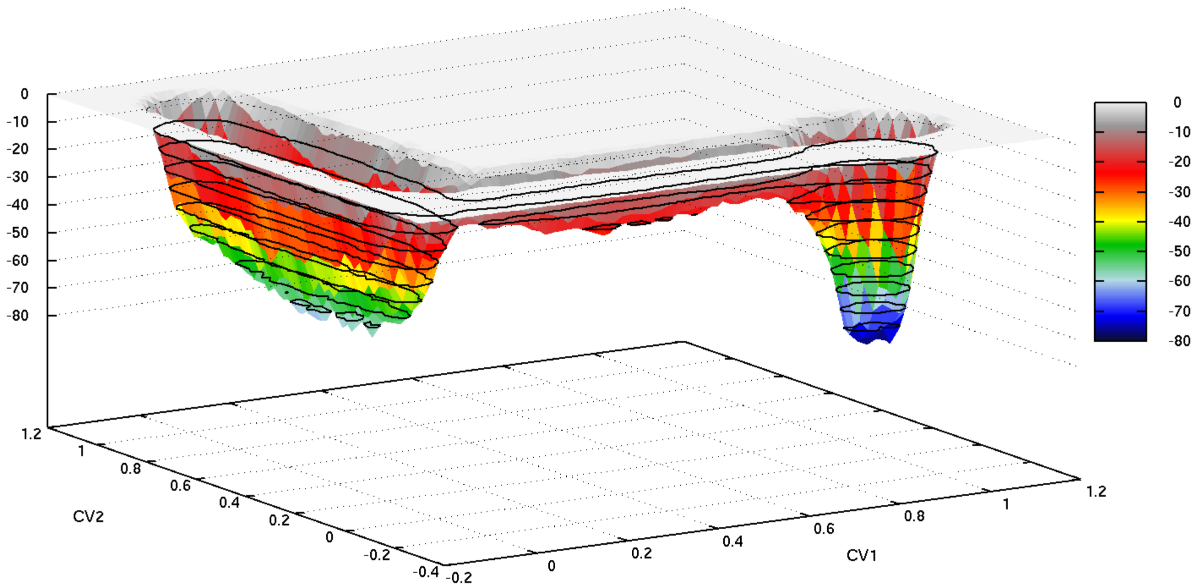

Figure 3: Free-energy surface (units in kJ/mol) for the proton-exchange reaction. X-axis is CV1 (CN of N to initial H) and Y-axis is CV2 (CN of N to all H_2O molecules).

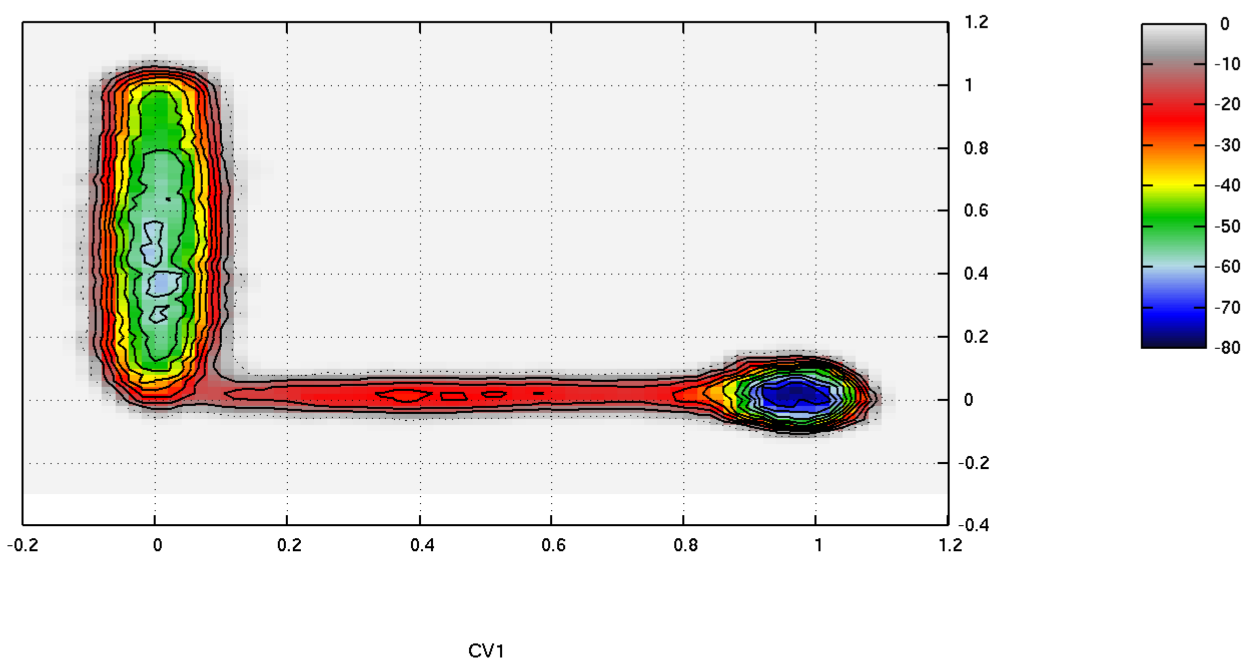

Figure 4: Contour plot of the free-energy (units in kJ/mol) for the proton-exchange reaction. X-axis is CV1 (CN of N to initial H) and Y-axis is CV2 (CN of N to all H_2O molecules).

ring, $\Delta(\lambda\lambda\lambda\lambda)$, unambiguously define the TSAP isomer. The nitrogen of the pyridine (N_{pyr}) is bound in the pseudo plane defined by the remaining three oxygen atoms (O1, O2, and O3) and forms with these three oxygen atoms a slightly distorted O3N square. The four nitrogens of the macrocycle form another pseudo plane (N4). The two N4 and O3N planes are parallel within 3.01 degrees and the angle ω formed by their mutual rotation is averaged at 15.4 degrees (ideal angle is 22.5 degrees for TSAP[31]). The Eu(III) ion is placed at 0.861 Å from the upper plane and 1.685 Å from the plane defined by the nitrogen atoms of the cyclen unit. The distance between the two planes is averaged at 2.51 Å, very close to the 2.52 Å reported for the TSAP form of DOTA.[32] The angles O_1-Eu-O_3 and N_{pyr}-Eu-O_2 are 141.1(1) and 136.24(9) degrees, respectively, closest from the angle of 144 degrees observed for the TSAP form of DOTA than the 148 degrees of its SAP form.[32] The capping position was occupied by the carbamate oxygen O_{carb} at a distance of 2.44 Å from the metal which is only 0.04 Å longer than the reported Gd-O distance (2.40 Å) for the capping water molecule in the Gd(III) complex carrying a non-substituted pyridine.[33] The Eu-N_{pyr} distance of 2.699 Å is significantly longer than the other bonds involving the cation such as remaining Eu-O bond lengths which averaged 2.371 Å. A similar behavior was reported for the sodium complex of DO3A carrying a bis picolyl amine substituted pyridine (Na-N: 2.797 Å).[34] However a shorter Ln-N distance was reported in the case of complexes carrying an unsubstituted pyridine[14] (2.53 Å) or a bidentate phenanthroline (2.55 Å).[35] The distances between the Eu and the four nitrogens of the macrocyle are not identical, as a consequence, the metal is not centered within the square N4. This may be due to the accommodation of the carbamate steric bulk and may weaken the coordination.

To compare with the *ab initio* metadynamics simulation, the analysis of the configurations extracted from the trajectory has to be restrained to the first free-energy basin, namely, to the first 1760 MD steps (see Figure 5). The corresponding distances are reported in Table 1. Not included in this table is the average N–O distance between the carbamate nitrogen and the hydrogen-bonded water molecule which is equal to 2.95 Å, i.e., slightly longer than in the unbiased CP trajectory. We note the good agreement between experimental and CP simulated Eu-N_{pyr} distances, which are significantly longer than for the coordinated oxygen atoms. There is however a general trend, namely that calculated distances are somewhat longer than the experimental ones. This could either stem from the fact that the aqueous solution at 310 K in the *ab initio* simulation is more diluted than in the crystal or from the use of large core pseudopotentials, which often slightly overestimate interatomic distances. The average N_{pyr}-Eu-O_2 and O_1-Eu-O_3 angles obtained from our simulation are 138 and 139 degrees, respectively, which are also in agreement with the X-ray values of 136 and 141 degrees.

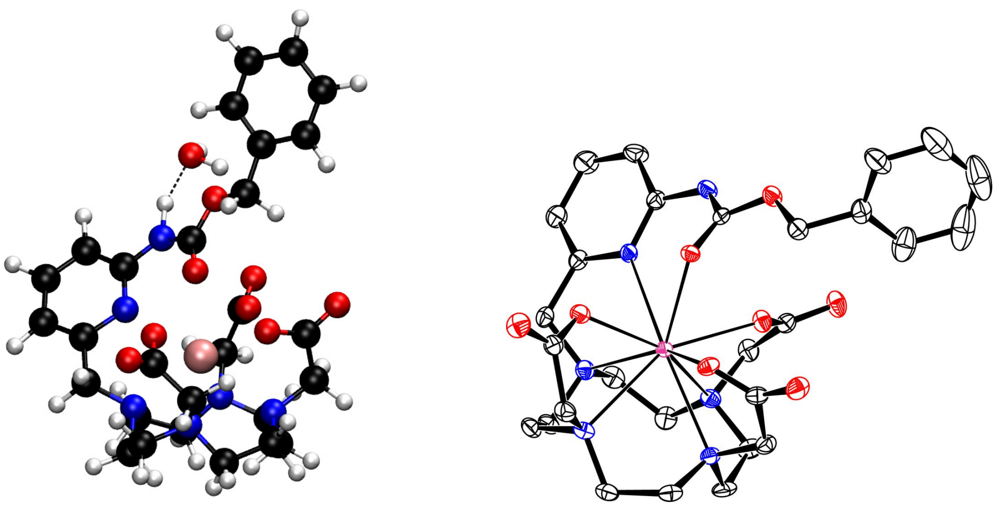

Figure 5: Left: typical configuration found in the first MTD free-energy basin (to make the picture clearer all solvent molecules have been erased except for the water molecule which is hydrogen-bonded to the NH group). Right: ORTEP-III plot[30] from X-ray diffraction (ellipsoids are drawn at the 30% probability level; waters and H atoms are not shown for clarity).

Reaction mechanism study

Following the minimum free-energy path between the two main basins obtained from our *ab initio* metadynamics simulation, the reaction mechanism for the proton exchange can basically be decomposed into nine steps (see Figure 6). Initially (in the first basin), a water molecule forms a hydrogen bond with the proton of the NH group (see picture (a)). Then

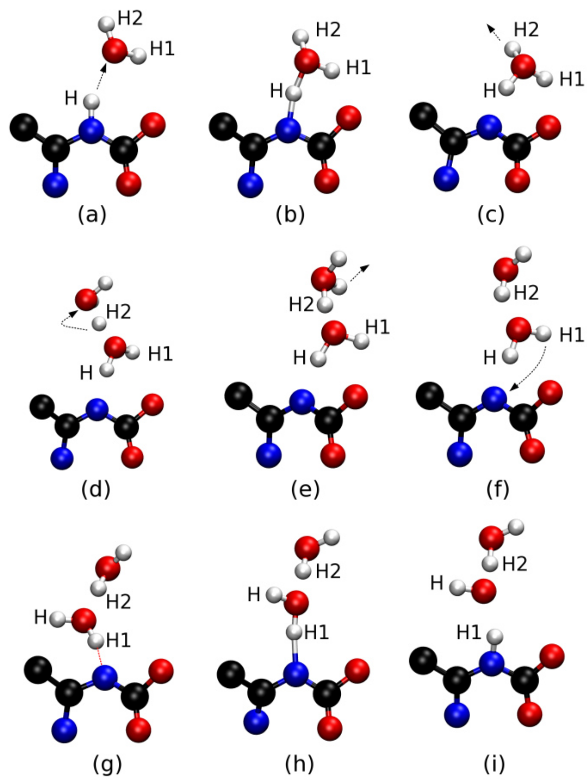

Figure 6: Reaction mechanism for the proton exchange (see text for explanation). Only the relevant atoms are represented.

the latter proton becomes shared between both molecules (see picture (b)). Crossing this transition state and entering the large intermediate region of the free-energy surface, the proton achieves its transfer onto the water molecule as depicted in picture (c), forming a H_3O^+ ion. Then one of the water protons (H2) detaches (see picture (d)) and jumps onto a second water molecule (see picture (e)), again forming a H_3O^+ ion. This causes the departure of one of its initial proton (see picture (f)). A cascade of proton transfers is actually triggered following structural Grotthuss diffusion,[36] which here involves up to five "wired" water molecules (see Figure 7). To reach the second basin, the first water

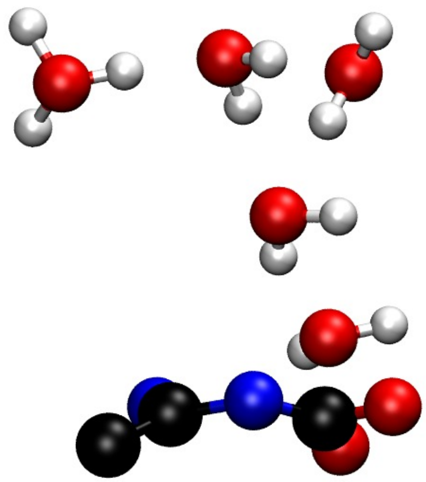

Figure 7: Chain of four water molecules plus one hydronium ion after Grotthuss diffusion (in comparison with previous pictures, the view is from the top). The fourth water molecule is actually hydrogen-bonded to a carboxylate oxygen of the paraCEST agent.

molecule reorientates so that proton H1 forms a hydrogen bond with the nitrogen atom (see picture (g)). The latter proton becomes shared between both molecules (see picture (h)) before it is transfered onto nitrogen, leaving an OH^- ion (see picture (i)). This configuration, close to (0.01,0.95) on the surface, is however approximately 30 kJ/mol above the global free-energy minimum and the hydroxide ion takes the proton back from the carbamate nitrogen.

The expected proton exchange reaction has therefore not been fully completed during our *ab initio* metadynamics simulation due to the absence of OH^- charge diffusion. A fine analysis of our tajectory reveals that this hydroxide ion actually accepts three strong hydrogen bonds (from two water molecules and the NH group) plus one weak hydrogen bond (from the closest CH group of pyridine), as depicted in Figure 8. This coordination pattern is actually reminiscent of the case of hydroxide ion in liquid water.[37] In this case, several factors that directly influence its migration dynamics have been identified. These are especially the choice of the exchange-correlation density functional[38] and nuclear quantum effects, that reduce the barrier height of the proton transfer process.[39] In addition, deuteration (that we have used to ensure Car-Parrinello simulation adiabaticity) results in smaller diffusion coefficients of OD^-.

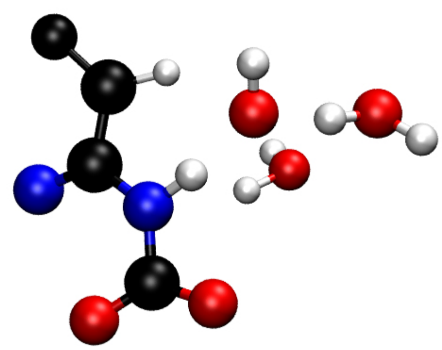

Figure 8: Configuration showing the four hydrogen bonds around the hydroxide ion (in comparison with previous pictures, the view is chosen so that the OH^- ion is almost axial).

In summary, our simulation shows that the mechanism of carbamate proton exchange in the lanthanide complex involves a fast diffusion of the H_3O^+ ion after the proton transfer from the carbamate nitrogen. This must be related to the kind of hydrogen bond that initially links both molecules, namely, oxygen being the proton acceptor. An alternative scenario would definitely occur if nitrogen would instead be the proton acceptor. It should be noted that no specific hydrogen-bonded network was favored at the beginning of our first CP simulation; the hydrogen bond between water and carbamate appeared spontaneously.

Conclusion

The understanding of the proton exchange rate, which is at the core of the CEST mechanism, has up to now been oversimplified due to experimental limitations and lack of high-level simulations. In this work, using accelerated *ab initio* simulation techniques, we take a step forward by reconstructing the free energy landscape of one of the isomers of a lanthanide-based paraCEST agent endowed with potential multimodality detection capabilities, and by unveiling the elementary steps of its proton exchange mechanism. A good agreement is found between experimental (on a mixture of SA and TSAP isomers) and theoretical (focused on the TSAP isomer) proton exchange free-energy barriers which suggests that the two isomers should have similar proton exchange rate constants.

A preliminary step to the proton exchange process is the formation of a strong hydrogen bond between the carbamate nitrogen and a water molecule. A cascade of proton transfers then occurs, following structural Grotthuss diffusion and leading to the formation of "wired" water molecules around the complex. However, the present simulation could not capture the diffusion of the OH^- charge necessary for the completion of the proton exchange.

Up to now, the efficacy of a CEST agent, determined mainly by its k_{ex}, cannot be predicted easily. The whole synthesis, very often time-consuming, of the complex has to be done, and k_{ex} has to be measured. The theoretical determination of the corresponding free-energy barrier can contribute to the design of more efficient CEST agents in an optimized timescale.

Acknowledgement

Most of the simulations were done using HPC resources from GENCI-IDRIS. We thank Agnès Pallier and Jean-François Gallard for their help in the experimental NMR work and Ewen Lescop for helpful discussions. The Ligue contre le cancer and ANR (ENZYMAGE) are acknowledged for financial support.

Supporting Information Available

The following files are available free of charge. Materials and methods, synthesis of the Europium complex, NMR analysis, HPLC traces, NMR spectra, crystallographic details, CEST Spectra. This material is available for download from `http://pubs.acs.org`

References

(1) Winter, P. M. Magnetic resonance chemical exchange saturation transfer imaging and nanotechnology. *WIRES Nanomed Nanobiotechnol* **2012**, *4*, 389-398.

(2) Hancu, I.; Dixon, W. T.; Woods, M.; Vinogradov, E.; Sherry, A. D.; Lenkinski, R. E. CEST and PARACEST MR contrast agents. *Acta Radiol.* **2010**, *51*, 910-923.

(3) Sherry, A. D.; Woods, M. Chemical exchange saturation transfer contrast agents for magnetic resonance imaging. *Annu Rev Biomed Eng* **2008**, *10*, 391-411.

(4) Woods, M.; Woessner, D. E.; Sherry, A. D. Paramagnetic lanthanide complexes as PARACEST agents for medical imaging. *Chem. Soc. Rev.* **2006**, *35*, 500-511.

(5) Zhang, S.; Merritt, M.; Woessner, D. E.; Lenkinski, R. E.; Sherry, A. D. PARACEST agents: modulating MRI contrast via water proton exchange. *Acc. Chem. Res.* **2003**, *36*, 783-790.

(6) Terreno, E.; Castelli, D. D.; Aime, S. Paramagnetic CEST MRI contrast agents. In *The Chemistry of Contrast Agents in Medical Magnetic Resonance Imaging*; Merbach, A. E.; Helm, L.; Toth, E., Eds.; Wiley, 2013; Chapter 9, pp 387–425.

(7) He, J.; Bonnet, C. S.; Eliseeva, S. V.; Lacerda, S.; Chauvin, T.; Retailleau, P.; Szeremeta, F.; Badet, B.; Petoud, S.; Toth, E.; Durand, P. Prototypes of lanthanide(III) agents responsive to enzymatic activities in three complementary imaging modalities:

visible/near-infrared luminescence, PARACEST-, and T1-MRI. *J. Am. Chem. Soc.* **2016**, *138*, 2913-2916.

(8) Pollet, R.; Marx, D. Ab initio simulation of a gadolinium-based magnetic resonance imaging contrast agent in aqueous solution. *J. Chem. Phys.* **2007**, *126*, 181102.

(9) Pollet, R.; Nair, N.; Marx, D. Water exchange of a ProHance MRI contrast agent: isomer-dependent free-energy landscapes and mechanisms. *Inorg. Chem.* **2011**, *50*, 4791-4797.

(10) Lasoroski, A.; Vuilleumier, R.; Pollet, R. Hyperfine interactions in a gadolinium-based MRI contrast agent: high-frequency modulations from ab initio simulations. *J. Chem. Phys.* **2013**, *139*, 104115.

(11) Lasoroski, A.; Vuilleumier, R.; Pollet, R. Vibrational dynamics of zero-field-splitting hamiltonian in gadolinium-based MRI contrast agents from ab initio molecular dynamics. *J. Chem. Phys.* **2014**, *141*, 014201.

(12) Laio, A.; Gervasio, F. L. Metadynamics: A method to simulate rare events and reconstruct the free energy in biophysics, chemistry and material science. *Rep. Prog. Phys.* **2008**, *71*, 126601.

(13) Laio, A.; Parrinello, M. Escaping free-energy minima. *Proc. Natl. Acad. Sci. USA* **2002**, *99*, 12562-12566.

(14) Nonius, B. V. COLLECT, data collection software, **1999**.

(15) Otwinowski, Z.; Minor, W. Processing of X-ray diffraction data collected in oscillation mode. *Methods in Enzymology*; Academic Press: New York, **1997**; p 307-326.

(16) Sheldrick, G. M. A short history of SHELX. *Acta Cryst.* **2008**, *A64*, 112-122.

(17) Sheldrick, G. M. Crystal structure refinement with SHELXL. *Acta Cryst.* **2015**, *C71*, 3-8.

(18) Parsons, S.; Flack, H. D.; Wagner, T. Use of intensity quotients and differences in absolute structure refinement. *Acta Cryst.* **2013**, *B69*, 249.

(19) Dixon, W. T.; Lubag, A. J. M.; Ratnakar, J.; Vinogradov, E.; Hancu, I.; Lenkinski, R. E.; Sherry, A. D. A concentration-independent method to measure exchange rates in PARACEST agents. *Magn. Reson. Med.* **2010**, *63*, 625-632.

(20) Randtke, E. A.; Chen, L. Q.; Corrales, L. R.; Pagel, M. D. The Hanes-Woolf linear QUESP method improves the measurements of fast chemical exchange rates with CEST MRI. *Magn. Reson. Med.* **2014**, *71*, 1603-1612.

(21) Perdew, J. P.; Burke, K.; Ernzerhof, M. Generalized gradient approximation made simple. *Phys. Rev. Lett.* **1996**, *77*, 3865, Erratum: (1997) Phys Rev Lett 78,1396.

(22) Vanderbilt, D. Soft self-consistent pseudopotentials in a generalized eigenvalue formalism. *Phys. Rev. B* **1990**, *41*, 7892.

(23) Grimme, S. Semiempirical GGA-type density functional constructed with a long-range dispersion correction. *J. Comp. Chem.* **2006**, *27*, 1787-1799.

(24) Car, R.; Parrinello, M. Unified approach for molecular dynamics and density-functional theory. *Phys. Rev. Lett.* **1985**, *55*, 2471.

(25) Marx, D.; Hutter, J. In *Modern Methods and Algorithms of Quantum Chemistry*; Grotendorst, J., Ed.; NIC: Jülich, 2000, pp 301 – 449, for downloads see `www.theochem.rub.de/go/cprev.html`.

(26) Stirling, A.; Iannuzzi, M.; Laio, A.; Parrinello, M. Azulene-to-naphthalene rearrangement: the Car-Parrinello metadynamics method explores various reaction mechanisms. *ChemPhysChem* **2004**, *5*, 1558-1568.

(27) Iannuzzi, M.; Laio, A.; Parrinello, M. Efficient exploration of reactive potential energy surfaces using Car-Parrinello molecular dynamics. *Phys. Rev. Lett.* **2003**, *90*, 238302.

(28) Laio, A.; Rodriguez-Fortea, A.; Gervasio, F. L.; Ceccarelli, M.; Parrinello, M. Assessing the accuracy of metadynamics. *J. Phys. Chem. B* **2005**, *109*, 6714-6721.

(29) Ensing, B.; Laio, A.; Parrinello, M.; Klein, M. L. A recipe for the computation of the free energy barrier and the lowest free energy path of concerted reactions. *J. Phys. Chem. B* **2005**, *109*, 6676-6687.

(30) Spek, A. L. Structure validation in chemical crystallography. *Acta Cryst.* **2009**, *D65*, 148-155.

(31) Hermann, P.; Kotek, J.; Kubicek, V.; Lukes, I. Gadolinium(III) complexes as MRI contrast agents: ligand design and properties of the complexes. *Dalton Trans.* **2008**, 3027-3047.

(32) Parker, D.; Dickins, R. S.; Puschmann, H.; Crossland, C.; Howard, J. A. K. Being excited by lanthanide coordination complexes: aqua species, chirality, excited-state chemistry, and exchange dynamics. *Chem. Rev.* **2002**, *102*, 1977-2010.

(33) Aime, S.; Batsanov, A. S.; Botta, M.; Howard, J. A. K.; Lowe, M. P.; Parker, D. Structure and relaxivity of macrocyclic gadolinium complexes incorporating pyridyl and 4-morpholinopyridyl substituents. *New J. Chem.* **1999**, *23*, 669-670.

(34) Pope, S. J. A.; and, R. H. L. Design, synthesis and photophysical studies of an emissive, europium based, sensor for zinc. *Dalton Trans.* **2006**, 3108-3113.

(35) Quici, S.; Marzanni, G.; Forni, A.; Accorsi, G.; Barigelletti, F. New lanthanide complexes for sensitized visible and near-IR light emission: synthesis, 1H NMR, and X-ray structural investigation and photophysical properties. *Inorg. Chem.* **2004**, *43*, 1294-1301.

(36) Marx, D. Proton transfer 200 years after von Grotthuss: insights from ab initio simulations. *ChemPhysChem* **2006**, *7*, 1848-1870.

(37) Tuckerman, M.; Laasonen, K.; Sprik, M.; Parrinello, M. Ab initio molecular dynamics simulation of the solvation and transport of H3O+ and OH- ions in water. *J. Phys. Chem.* **1995**, *99*, 5749-5752.

(38) Tuckerman, M. E.; Chandra, A.; Marx, D. Structure and dynamics of OH-(aq). *Acc. Chem. Res.* **2006**, *39*, 151-158.

(39) Marx, D.; Tuckerman, M.; Parrinello, M. The nature and transport mechanism of hydrated hydroxide ions in aqueous solution. *Nature* **2002**, *417*, 925-929.

Graphical TOC Entry

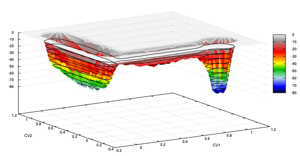

A combined theoretical and experimental study of a paramagnetic chemical exchange saturation transfer agent sheds light on the proton-exchange reaction. Its mechanism involves structural Grotthuss diffusion. *Ab initio* simulation techniques are shown to contribute to the design of more efficient CEST agents.